BIOCHEMISTRY

Structures of human pannexin-1 in nanodiscs reveal gating mediated by dynamic movement of the N terminus and phospholipids

Maki Kuzuya[1], Hidemi Hirano[2], Kenichi Hayashida[2], Masakatsu Watanabe[3], Kazumi Kobayashi[4], Tohru Terada[5], Md. Iqbal Mahmood[6], Florence Tama[6,7,8], Kazutoshi Tani[9], Yoshinori Fujiyoshi[10,11], Atsunori Oshima[1,2,12]*

Pannexin (PANX) family proteins form large-pore channels that mediate purinergic signaling. We analyzed the cryo-EM structures of human PANX1 in lipid nanodiscs to elucidate the gating mechanism and its regulation by the amino terminus in phospholipids. The wild-type channel has an amino-terminal funnel in the pore, but in the presence of the inhibitor probenecid, a cytoplasmically oriented amino terminus and phospholipids obstruct the pore. Functional analysis using whole-cell patch-clamp and oocyte voltage clamp showed that PANX1 lacking the amino terminus did not open and had a dominant negative effect on channel activity, thus confirming that the amino-terminal domain played an essential role in channel opening. These observations suggest that dynamic conformational changes in the amino terminus of human PANX1 are associated with lipid movement in and out of the pore. Moreover, the data provide insight into the gating mechanism of PANX1 and, more broadly, other large-pore channels.

INTRODUCTION

Pannexin (PANX) is a member of the mammalian channel protein family with an amino acid sequence that is partially homologous with the innexin family of gap junction proteins in invertebrates. The PANX family comprises three isoforms, referred to as PANX1, PANX2, and PANX3 (*1*), and these channels are associated with purinergic signals, such as in inflammation, cancer progression, synaptic transmission, and epilepsy (*2*–*4*). PANX1 has been the most studied and is the best characterized. In most cancer cells, PANX1 proteins are up-regulated (*5*). A gain-of-function mutation in PANX1 increases metastasis of breast cancer cells (*6*), and PANX1 inhibition reduces melanoma cell growth and migration (*7*). Thus, controlling PANX1 activity may be a promising strategy for cancer treatment. The gout treatment probenecid (PBN) inhibits PANX1 channel activity (*8*) and is suggested to interact with the first extracellular loop of PANX1 (*9*).

PANX1 has four transmembrane helices that generate different conductance levels (around 100 to 500 pS) in different systems, including lipid bilayer recordings, mammalian cells, and *Xenopus* oocytes, depending on whether the C-terminal tail is intact or truncated (*10*–*13*), with a permeant size of up to ~1.0 kDa (*14*). This pore size is large enough to permeate ions, metabolites, and second messengers such as adenosine triphosphate (ATP). High-resolution structures of PANX1 determined by cryo–electron microscopy (cryo-EM) (*15*–*19*) revealed that a single channel comprises heptameric subunits with a pore size in the transmembrane region of over 15 Å but that the extracellular loop forms a narrow constriction. The overall architecture of PANX1 is consistent with that of other large-pore channels, such as volume-regulated anion channels and gap junction channels (*20*–*22*), but the subunit number is variable. The helical arrangement in a subunit of the above-mentioned channels is opposite that of calcium homeostasis modulator (CALHM) channels, another family of large-pore channels (*23*–*26*). In many PANX1 structures, the N-terminal end is partially disordered and oriented to the cytoplasmic side, but only a single report has assigned the N-terminal region to the second residue as a funnel configuration in the pore. On this basis, it has been proposed that the side tunnels may be gated independently from the main pore (*16*).

Phospholipids are often visualized in high-resolution structures of membrane channels. In tetrameric ion channels, lipid alkyl chains have been visualized in x-ray crystal structures of tandem of P-domains in a weakly inward rectifying K^+ channel (TWIK-1), TWIK-related arachidonic acid–stimulated K^+ channel (TRAAK), and voltage-gated Na^+ channel from *Arcobacter butzleri* (NavAb) (*27*–*29*), where the side fenestrations are partially occupied. Findings from cryo-EM studies have led to the proposal that the innexin-6 (INX-6) hemichannel pore in a nanodisc is filled with phospholipids and that the N-terminal domains are rearranged to close the channel (*30*). A similar interpretation has been proposed for the lipid-like densities in the pore pathway of CALHM2 and CALHM4 (*24*, *31*). These structural studies suggest that lipid gating, or the influx of phospholipids into the pore, is essential for complete closure of these channels.

Previous structural studies of PANX1 did not clarify the conformational change between the open and closed states in lipid bilayers. In the present study, we investigated the structures of nanodisc-reconstituted PANX1 with cryo-EM. High-resolution structures of PANX1 were determined under four conditions: wild type (WT PANX1),

[1]Department of Basic Medicinal Sciences, Graduate School of Pharmaceutical Sciences, Nagoya University, Furo-cho, Chikusa-ku, Nagoya 464-8601, Japan. [2]Cellular and Structural Physiology Institute (CeSPI), Nagoya University, Furo-cho, Chikusa-ku, Nagoya 464-8601, Japan. [3]Graduate School of Frontier Biosciences, Osaka University, 1-3 Yamadaoka, Suita, Osaka 565-0871, Japan. [4]JEOL Ltd., 3-1-2 Musashino, Akishima, Tokyo 196-8558, Japan. [5]Department of Biotechnology, Graduate School of Agricultural and Life Sciences, University of Tokyo, 1-1-1 Yayoi, Bunkyō-ku, Tokyo 113-8657, Japan. [6]Department of Physics, Graduate School of Science, Nagoya University, Furo-cho, Chikusa-ku, Nagoya 464-8601, Japan. [7]Institute of Transformative Bio-Molecules (WPI-ITbM), Nagoya University, Furo-cho, Chikusa-ku, Nagoya 464-8601, Japan. [8]RIKEN Center for Computational Science, Kobe, Hyogo 650-0047, Japan. [9]Graduate School of Medicine, Mie University, 2-174 Edobashi Tsu, Mie 514-8507, Japan. [10]Advanced Research Institute, Tokyo Medical and Dental University, 1-5-45 Yushima, Bunkyō-ku, Tokyo 113-8510, Japan. [11]CeSPIA Inc., Otemachi, Chiyoda, Tokyo 100-0004, Japan. [12]Institute for Glyco-core Research (iGCORE), Nagoya University, Furo-cho, Chikusa-ku, Nagoya 464-8601, Japan.
*Corresponding author. Email: atsu@cespi.nagoya-u.ac.jp

WT with 3 mM PBN (PANX1-PBN), N-terminal–deleted PANX1 (PANX1ΔN20), and C-terminal–deleted PANX1 (PANX1ΔC379). Two structural states, possibly open and closed, of PANX1 were obtained, revealing a distinctive conformational change in the N terminus and phospholipid distribution in the pore. *Xenopus* oocytes were voltage-clamped, and human embryonic kidney (HEK) cells were patch-clamped to analyze activity. Our observations provide an interpretation of the gating mechanism of the PANX1 channel in which phospholipid distribution in the pore is critical for channel blockade, similar to the lipid-gating mechanism reported in other large-pore channels.

RESULTS

Cryo-EM structure of WT PANX1 in a nanodisc reveals the N-terminal funnel

Human WT PANX1 conjugated with the C-terminal green fluorescent protein (GFP)–8His tag were expressed in Expi293 cells and purified by affinity and size exclusion chromatography (fig. S1A). The purified WT PANX1 channels were reconstituted in lipid nanodiscs with the membrane scaffold protein MSP2N2 and 1-palmitoyl-2-oleoyl-sn-glycero-3-phosphocholine (POPC). After confirming that the nanodisc particles were well dispersed in negatively stained electron micrographs (fig. S1B), cryo-EM data of WT PANX1 were collected (fig. S1C).

The cryo-EM structure of WT PANX1 was determined at 3.6-Å resolution (figs. S1, D to G, and S2A and table S1). A complete PANX1 channel contains seven subunits with dimensions of about 98 Å in the horizontal plane and 106 Å in the vertical plane (Fig. 1, A and B). The N terminus starts at the second residue, Ala^{2}, because we confirmed by protein sequencing that the first methionine residue was cleaved by proteolysis (fig. S3, A and B). The cytoplasmic loop and C-terminal domain are partially disordered, resulting in missing residues from Ser^{159} to Tyr^{193} and after Ser^{357}. The PANX1 monomer contains the following secondary structures: the N-terminal helix (NTH), four transmembrane helices (TM1 to TM4), five helical segments in the cytoplasmic domain (CH1 to CH5), and three helical domains and β strands in the extracellular domain (Fig. 1C and fig. S4). As usually found in gap junction family proteins, two disulfide bonds are formed between the extracellular loops E1 and E2 (fig. S5A). This organization is consistent with other published PANX1 structures (*15*–*18*) and similar to those of Cx26 and INX-6 gap junction channels (*21*, *22*) and volume-regulated anion channels (*20*, *32*, *33*).

The N-terminal region, including NTH, forms a funnel configuration with a wide pore diameter of 17 Å and an entrance pore diameter of over 40 Å at the cytoplasmic side (fig. S5, B to D). A more constricted site with a diameter of 7.8 Å is located at the extracellular domains at Trp^{74} where unassigned densities are observed in the middle of both C7 (seven-fold cyclic) and C1 (no symmetry) maps (fig. S5E), suggesting that this is not due to the artificial effects caused by rotational symmetry operations. This position is postulated to be the carbenoxolone-binding site [Protein Data Bank (PDB)

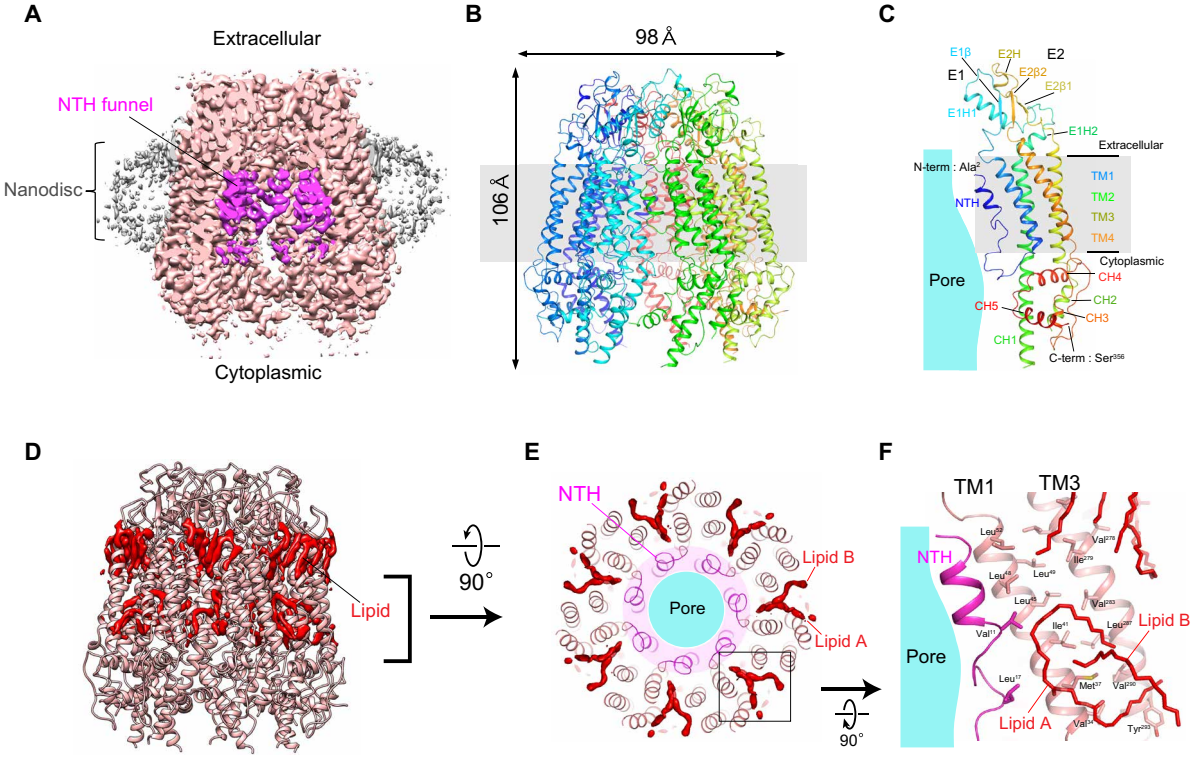

Fig. 1. Cryo-EM structure of WT PANX1 in a nanodisc. (**A**) A 3.6-Å resolution density map of WT PANX1 in a nanodisc viewed along the membrane plane. The NTH funnel and lipid nanodisc are colored magenta and gray, respectively. (**B**) Ribbon representation of the heptameric WT PANX1 model with each subunit is color coded. The lipid bilayer is shown in gray. (**C**) Monomeric structure of WT PANX1. NTH faces the pore that is colored cyan. The cytoplasmic loop and C terminus are mostly disordered. (**D**) Distribution of lipid densities in the WT PANX1 model. Lipid densities are shown in red in surface style. (**E**) Sectioned top view with 20-Å slab thickness indicated by the bracket in (D). Two lipids, A and B, are prevented from accessing the pore (cyan) by NTH (magenta). (**F**) Modeled lipids in the space between the adjacent transmembrane helix bundles. The boxed area in (E) is viewed along the membrane plane. Lipids, NTH, and the pore are colored as in (E).

code: 6wbf, EMD-21150] (*9*, *16*, *32*). Our structure, as well as the PANX1 structures from other groups (*15*, *17*, *19*), was solved without a blocker but still shows the unassigned density. Thus, it should be carefully considered whether this density corresponds to a blocker.

The three-dimensional (3D) reconstruction of WT PANX1 contains visible lipid densities (Fig. 1D). Specifically, the crevices in the subunit interfaces of adjacent transmembrane domains are occupied by at least two lipid molecules (Fig. 1E), and these are possibly carried over lipids from cultured cells because the structures of PANX1 in detergent demonstrate lipid densities in these crevices (*16*, *17*). The lipids in this cavity are surrounded by hydrophobic side chains (figs. S4 and S5F). The crevice is sealed by the NTH and connecting loop where Val^{11} and Leu^{17} face the lipids (Fig. 1, E and F). The lipids cannot access the pore because the N-terminal funnel surrounding the aqueous pore is in the way. There is no intersubunit polar interaction through the N-terminal domain. Instead, NTH is stabilized by hydrophobic interactions with TM1 of the same subunit and with TM2 of the adjacent subunit (fig. S5G). This arrangement is consistent with those of Cx46 and Cx50 (*34*) but contrasts with that of Cx26 (*21*), in which the N-terminal funnel is stabilized by the hydrogen bond network.

Pharmacological blockade of PANX1 rearranges the N termini and pore lipids

We next used the PANX1 blocker PBN to determine the structure of PANX1 in a closed conformation. PBN was added to the nanodisc-reconstituted WT PANX1 solution at a final concentration of 3 mM, well above the concentration that is sufficient to abolish the activity of WT PANX1 channel (1 mM) (*8*). The cryo-EM structure with PBN, referred to as PANX1-PBN, was determined at 3.4-Å resolution (Fig. 2, A and B; figs. S2B and S6A; and table S1). The overall architecture of PANX1-PBN is similar to that of WT PANX1: The root mean square deviation of Cα carbons, except for the N-terminal 29 residues, is 1.41 Å between the two PANX1 monomers. Because up to 12 residues from the N-terminal end are disordered, no helical feature for NTH is observed. As with WT PANX1, the C terminus was modeled up to Ser^{356}. Although the PBN binding site has been speculated to be in E1 (*9*, *35*), the density for PBN could not be identified in the PANX1-PBN map. The most prominent difference from WT PANX1 was that the PANX1-PBN N-terminal portion bends toward the cytoplasmic side like a whip (Fig. 2C). Arg^{29} is the pivot for the two N-terminal conformations, and more hydrogen bonds are formed in PANX1-PBN (fig. S6B), which may be associated with the N-terminal domain oriented to the cytoplasmic side. The N-terminal end, Ser^{13}, is surrounded by the C-terminal tail and the cytoplasmic loop, although there are only a few polar interactions (fig. S6C).

The tilt angle of the subunit relative to the membrane plane of PANX1-PBN differed from that of WT

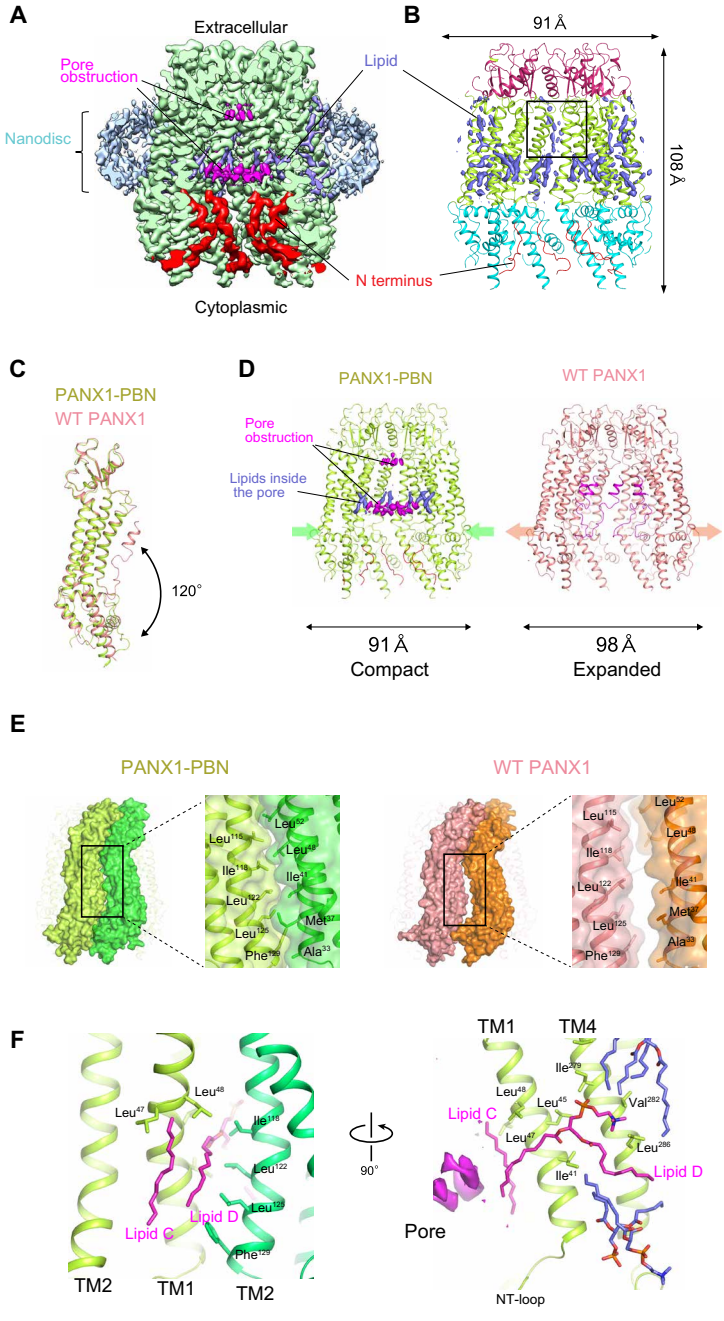

Fig. 2. Cryo-EM structure and atomic model of PANX1-PBN. (**A**) Gaussian-filtered cryo-EM density map of PANX1-PBN at 3.4-Å resolution. (**B**) Ribbon style atomic model of PANX1-PBN. The cytoplasmic, transmembrane, and extracellular regions are colored in cyan, green, and pink, respectively. The N-terminal loops are shown in red. The slate blue densities represent lipids around the transmembrane helices. The boxed region is magnified in (F). (**C**) N-terminal conformational change between WT PANX1 and PANX1-PBN. The N terminus of WT PANX1 is oriented to the cytoplasmic side in PANX1-PBN with a bending angle of 120°. (**D**) Compact and expanded conformational arrangement of transmembrane domains in PANX1-PBN and WT PANX1, respectively. (**E**) Subunit interfaces between PANX1-PBN and WT PANX1. Two subunits represented in surface view for PANX1-PBN (left) and WT PANX1 (right) reveals a wider interface space for WT PANX1. The boxed area is magnified and shown on the right. The side chains facing the interface of adjacent transmembrane helix bundles are drawn in stick style. (**F**) Magnified view of the boxed region in (B) to show the lipid distribution in the PANX1-PBN structure. Lipids on the intersubunit interfaces in the transmembrane domains are shown in red in stick style. Lipid C and part of lipid D are located in the pore of the channel, facing the pore obstruction density (magenta).

PANX1. Each subunit of PANX1-PBN is more perpendicular to the membrane plane, with the extracellular loop acting as fulcrum support and the cytoplasmic half of the transmembrane domain and the cytoplasmic loops of PANX1-PBN shifting toward the insides of the pore (Fig. 2D and movie S1). For example, the difference in distance for the cytoplasmic end residues is about 4.9 Å for Ala^{131} in TM2, 5.3 Å for Lys^{212} in TM3, 3.1 Å for Lys^{36} in TM1, and 3.8 Å for Val^{292} in TM4 (fig. S6D). These differences result in the wide space between the PANX1-PBN subunit interfaces of transmembrane helix bundles (Fig. 2E). Consequently, the outer dimension parallel to the membrane plane of PANX1-PBN is smaller by 8 Å as compared to that for WT. In terms of the N-terminal conformation, WT PANX1 is almost identical to the apo PANX1 structure in detergent (*16*), and the PANX1-PBN structure is similar to that for frog PANX1 (fig. S7, A and B, and table S2) (*15*). In contrast, the tilt angle of the PANX1-PBN subunits is similar to that in CBX-bound PANX1ΔC (fig. S7C) (*16*).

Densities corresponding to lipids are found around the subunits of PANX1-PBN (Fig. 2B and fig. S6E). Lipids were not only distributed in the interfaces between adjacent transmembrane helix bundles but also distributed inside the pore along TM1 (Fig. 2F and fig. S6F). In addition, the pore is obstructed by double-layer densities along the membrane plane (Fig. 2, A and D), suggesting a closed pore, which is reminiscent of the INX-6 gap junction hemichannel structures in nanodiscs (*30*). These observations suggest that lipid molecules would be able to pass through the intersubunit interface between the adjacent transmembrane domains with the N-terminal conformational change concurrently evoked in nanodiscs. Although the density corresponding to PBN was not identified in the cryo-EM map, an unassigned density was found on the extracellular pore axis, which was surrounded by Trp^{74} (fig. S6G). This position is the only place in the pore that is less than 15 Å in diameter (fig. S6H), but this extracellular density is commonly identified in both WT PANX1 and PANX1-PBN.

Structural similarity of N- or C-terminal deletion mutants to PANX1-PBN or WT PANX1

The N terminus is postulated to be indispensable for normal functionality of connexin and innexin gap junction channels (*30*, *36*). For PANX1, the importance of the C-terminal is suggested by the constitutive activity of the channel when the C terminus is cleaved (*37*). To investigate the roles of the N- and C-terminals in the PANX1 structure, we determined the cryo-EM structures of the N-terminal deletion mutant of PANX1ΔN20 and the C-terminal deletion mutant of PANX1ΔC379 at resolution of 4.5 and 3.6 Å, respectively (fig. S2, C and D, and table S1). The PANX1ΔN20 structure was in good agreement with PANX1-PBN, except that the N-terminal loop residues ahead of Phe^{20} are missing. The inside of the PANX1ΔN20 pore is filled with acyl chain–like densities, and the pore diameter profile is similar to PANX1-PBN (figs. S8A and S9A), whereas the structure of PANX1ΔC379 is similar to that of WT PANX1 in terms of the channel dimension and an N-terminal pore funnel with a diameter of over 17 Å (figs. S8B and S9B). The helix tilt angle to the membrane plane was also consistent between PANX1 WT and PANX1ΔC379 and between PANX1-PBN and PANX1ΔN20, indicating that PANX1ΔC379 had a wider subunit angle than PANX1ΔN20 (fig. S8, C and D).

Functional assays in whole-cell patch-clamped HEK cells and voltage-clamped oocytes

To confirm the functionality of the PANX1 channels used for cryo-EM analyses, we next performed functional assays using these constructs expressed in HEK cells. Voltage-dependent current was produced by WT PANX1 and PANX1ΔC379, but PANX1ΔC379 had five times higher conductivity than WT at a membrane potential of 150 mV (Fig. 3, A and B, and fig. S10), indicating that the C-terminal deletion reinforces the activity of PANX1. PANX1ΔN20, however, did not exhibit a positive current at all (Fig. 3A). The ΔN20 and ΔC379 double mutant (PANX1ΔN20ΔC379) also produced no current (Fig. 3A), suggesting that the N-terminal deletion acts in a dominant negative manner.

Because of the small current values from HEK cells, we also performed *Xenopus* oocyte voltage clamp experiments in which larger currents were detectable. In oocyte voltage clamp experiments, the WT PANX channels exhibited voltage-dependent positive currents that were substantially inhibited by 1 mM PBN at 60-mV membrane voltage (Fig. 3C and fig. S10). PANX1ΔC379 produced much larger currents than WT, as consistently found in HEK cells, but were still inhibited by PBN (Fig. 3D). This finding suggests that the PBN binding site is not distributed in the deleted C terminus (379 to 426). Note that oocytes injected with PANX1ΔC379 were almost dead within 48 hours after injection, whereas those injected with WT PANX1 survived longer. This finding is consistent with the notion that PANX1ΔC379 channels are constitutively active, as previously reported (*37*). On the other hand, no positive current was observed from PANX1ΔN20 (Fig. 3E). Because the functionality of PANX1ΔN20 was not rescued by the PANX1ΔN20ΔC379 double mutation and the activity of WT PANX1 was suppressed by coexpression with PANX1ΔN20 (Fig. 3, A and E), the N-terminal 20 residues, which are directly involved in the funnel configuration, are crucial for normal PANX1 channel function. The dominant negative property of N-terminal deletion has also been observed for INX-6 hemichannels (*30*) and other connexin gap junction channels (*36*, *38*). All the PANX1 proteins reached the surface of the HEK cells and oocytes, although some cells exhibited granule signals in the cytoplasm (fig. S11, A and B), confirming that peptides can be transported through the trans-Golgi network. These functional studies may correlate with the N-terminal pore funnel found in WT PANX1 and PANX1ΔC379 and the lipid-like density blocking the pore seen in PANX1-PBN and PANX1ΔN20 in our structural study.

Mutational analysis and molecular dynamics simulation of PANX1

Because our cryo-EM structures of PANX1 demonstrated that lipids are located in the intersubunit crevices (Figs. 1, E and F, and 2, B and F), we investigated the residues in TM1 and TM2 that are associated with the protein-lipid interactions. The channel activity of four point mutants (I41S, L45S, I118S, and L122S) was examined with oocyte voltage clamp experiments. The I41S, L45S, and L122S mutants had significantly larger currents than WT, and all these currents were PBN sensitive, including I118S, which did not show a clear difference (fig. S12). When the N terminus was deleted, all four mutants were nonfunctional, consistent with the lack of activity of PANX1ΔN20 (fig. S12). These suggest lateral movement of lipids between subunits if the reduced hydrophobicity due to the substitution to serine restricts lipid influx into the pore.

We further used molecular dynamics (MD) simulations to trace the lipid movement. The structures of WT PANX1 and PANX1-PBN were embedded in the lipid bilayer comprising POPC phospholipids, and lipids were additionally placed in the intersubunit crevices based on the cryo-EM structures. After the 1-μs calculation, lipids at the

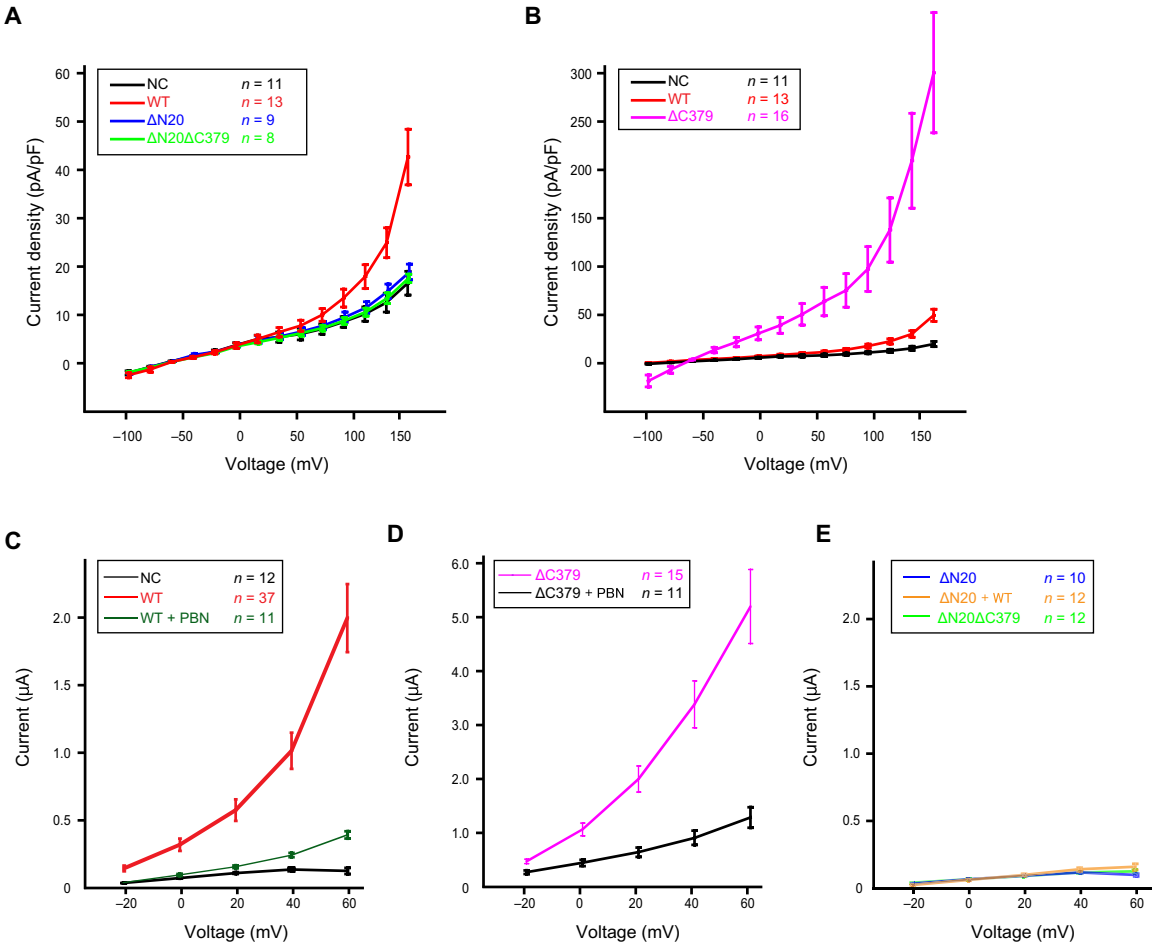

Fig. 3. Electrophysiology analyses to study the functionality of PANX1 channels. (**A** and **B**) Mean currents by whole-cell patch-clamp measurements of PANX1 channels in HEK293 cells. Currents of the negative control (NC; black), WT PANX1 (WT; red), PANX1ΔN20 (ΔN20; blue), and double-mutant PANX1ΔN20CΔ379 (ΔN20ΔC379; green) are plotted in (A). The currents of PANX1ΔC379, WT PANX1, and NC are plotted in (B). *N* values given in the panels represent the number of cells analyzed. Error bars: SE. (**C** to **E**) Voltage clamp currents of PANX1 in *Xenopus* oocytes. *I*/*V* plot for NC, WT, and WT with 1 mM PBN are shown in (C). PANX1ΔC379 and PANX1ΔC379 with 1 mM PBN are in (D), and PANX1ΔN20, coexpressed PANX1ΔN20 and WT PANX1, and the double-mutant PANX1ΔN20ΔC379 are in (E). *N* values given in the panels represent the number of cells analyzed. Error bars: SE.

subunit interface of WT PANX1 moved toward the pore (fig. S13 and movie S2). Lipid hydrocarbon chains inside the pore of PANX1-PBN were inserted into the interface between the subunits, and another lipid left the crevice (fig. S13 and movie S2). These results indicate that lipids may move thermodynamically through the intersubunit interfaces to enter and exit the pore of PANX1.

DISCUSSION

In this study, we present high-resolution structures of human PANX1 channels in lipid nanodiscs and two configurations from four structures. Several groups reported PANX1 structures in different configurations using cryo-EM (*15*–*19*). Of these structures, the N-terminal funnel of WT PANX1 in this study was also observed in the apo PANX1 structure in detergent (*16*). The N-terminal funnel found in connexin and innexin gap junction channels (*21*, *22*, *34*) has been interpreted to be an open form. Similarly, in combination with our functional results, the N-terminal funnel formed in the WT PANX1 structure suggests an open conformation.

Because the PBN density is not present in the PANX-PBN structure, it is unclear whether the conformation of PANX1-PBN is directly fixed by PBN or indirectly by other factors. We presume that PANX1-PBN is closed because the functionality of the channel is suppressed by PBN and the pore pathway is filled with densities of lipids and the double-layer pore obstruction, which was similarly observed in the structure of the loss-of-function mutant PANX1ΔN20. A straightforward interpretation for the pore-obstructing density is that lipids arranged in a bilayer appear to be visible in the pore (Fig. 4). Lipids surround the newly synthesized PANX1 monomer in the membrane, and thus lipids could be located inside the pore when the oligomer is formed. The pore lipids would not be excluded if the N terminus has been deleted, resulting in nonfunctionality. Lipid or lipid-like densities have also been identified in the pores of INX-6, Cx31.1, and CALHM channels (*24*, *30*, *31*, *39*), for which a lipid-gating model has been proposed (*24*, *30*). It is assumed that a similar closure model involving lipid blockage applies to PANX1 (Fig. 4). For membrane channels with a pore diameter of over 15 Å, a challenging issue is how to accomplish complete closure against

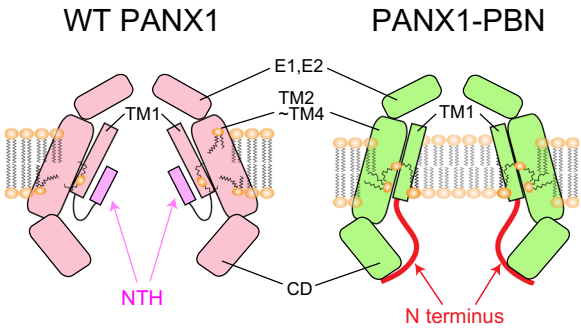

Fig. 4. Lipid-induced blockade of PANX1. In the N-terminal pore funnel configuration, the NTHs are stabilized in the pore to form a wide pathway, and lipids cannot reach the pore (left). In the lipid-induced blocked form, the N termini are oriented to the cytoplasmic side, and at the same time, the subunit interfaces widen, creating the intersubunit space in the transmembrane domain. When lipids are distributed in the pore, it is completely blocked, excluding the passage of hydrated ions (right). CD, cytoplasmic domain.

permeants. For PANX1, the cytoplasmic-oriented N termini would not be sufficient to prevent hydrated ions from passing through the pore (Fig. 2A and fig. S6H). If lipids can be placed in the pore, however, then complete pore closure would be possible (Fig. 4). In addition, the lipid-induced blockage accounts for the dominant negative property of PANX1ΔN20 (Fig. 3, A and E). Because the C-terminal domains are not resolved in the structure of WT PANX1, we cannot exclude the possibility that the unresolved C terminus contributes to the pore obstruction densities. Note also that blocker-induced closure may not represent a physiologically closed conformation. The structural study of PANX1 under more conditions that more closely replicate biological conditions, such as in proteoliposomes, will be necessary to investigate the intrinsic functionality of PANX1.

It has been reported that PANX1 is inactive unless the C terminus is cleaved by caspase (*13*, *37*), although intact PANX1 channels show weak voltage-dependent activity (*9*). Caspase-induced C-terminal cleavage, which is not reversible, may not be involved in physiological ATP release, which is reversible. One possibility is that caspase cleavage may occur in specific biological contexts because the original report of PANX channel activity demonstrates voltage-dependent positive current (*40*). Truncating the C terminus by ~70 residues still keeps PANX1 channels closed at holding potential but open depending on voltage (*41*). These discrepancies remain to be resolved by further investigation.

In lipid-induced channel blockade, it remains unclear where the lipids come from and how the lipids escape when the pore opens. For PANX1, the most plausible pathway is the crevice between the adjacent transmembrane helix bundles, where visible lipid acyl chains are similarly distributed in our PANX1 structures and those of others (Fig. 2F) (*16*, *17*). In the PANX1 transmembrane domains, there are no prominent intersubunit interactions because of the inserted lipids. Conformational changes to PANX1 subunits that alter their spacing (Fig. 2E) may result in the migration of lipids through the hydrophobic amino acid residues. Our mutant analyses and MD simulations indirectly support this idea (figs. S12 and S13 and movie S2). A similar wide space flanked by adjacent subunits is observed in INX-6 structures containing unassigned densities (*22*, *30*). The wider subunit interface space of WT PANX1 compared to that of PANX1-PBN (Fig. 2E) is reminiscent of the loose and tight interfaces of leucine-rich repeat-containing protein 8 (*33*). It remains to be elucidated whether the dynamic N-terminal movement is related to the lipid influx into the pore, as well as the energy source for the N-terminal conformational change. It is also unclear whether the hypothesized lipid movement is reversible, which may be resolved by the cryo-EM structure of PANX1 after removal of PBN. The cleavage of the C-terminal tail by caspase-7 results in a constitutively opened pore (*37*) and therefore would not be reversible. Because the N-terminal tail of PANX1-PBN is close to the unassigned C-terminal portion, these terminal domains may interact in such a way as to trigger N-terminal rearrangement.

Gap junction and related channel proteins have also been determined by cryo-EM in rapid succession (*22*, *24*, *30*, *31*, *34*, *39*). Although the amino acid sequences of these proteins do not always have substantial homology, they commonly form large pores of over 10 Å in diameter at the pore-lining N terminus. Although the gating mechanisms of these channels may vary, our observations provide a possible interpretation for large-pore channels in which lipids play a major role in the pore channel closing mechanism. The N terminus has been postulated to not be required for gating but rather for maintaining the large pore (*16*). For CALHM channels, an alternative protein gate model in which NTH and TM1 physically block the pore has been proposed (*23*–*25*). Our functional assays support the requirement of the N terminus for PANX1 function in HEK cells and oocytes (Fig. 3, A to E), which is consistently observed in gap junction family proteins (*36*, *42*, *43*). At present, it may be difficult to consolidate the gating mechanism of the large-pore channels into a single model, and it would not be surprising whether distinctive gating mechanisms exist. In cells, channels function in the presence of membrane potential. An experimental design that takes membrane potential into account is necessary to address this challenging interpretation. To precisely understand the gating mechanism of these channels, elucidation of protein-lipid interactions with cryo-EM will be increasingly important.

MATERIALS AND METHODS

Expression and purification of PANX1

Human PANX1 with the C-terminal tag containing GFP and 8x-histidine was subcloned in the BacMam expression vector (*44*). PANX1ΔN20 with the N-terminal deletion of residues 2 to 20 and PANX1ΔC379 with the C-terminal deletion of residues 380 to 426 were generated with a site-directed mutagenesis protocol. The recombinant baculovirus was amplified twice in insect Sf9 cells and used to infect Expi293 cells for protein expression. Expi293 cells were cultured at 37°C in 5% CO_2. The virus-infected Expi293 cells were harvested 48 hours after infection. The following processes were all performed at 4°C unless otherwise noted. The cells were disrupted by homogenizing in buffer containing 50 mM Hepes (pH 7.5), 300 mM NaCl, 0.2% digitonin, and 10% glycerol. The suspension was centrifuged at 500*g* for 5 min, and the supernatant was centrifuged at 118,000*g* for 30 min. The pelleted membrane fraction was solubilized in buffer containing 50 mM Hepes (pH 7.5), 300 mM NaCl, 1 mM EDTA, and 2% digitonin for 40 min on a circular rotator. The debris was removed by centrifugation at 15,300*g* for 10 min. The supernatant was bound to Ni–nitrilotriacetic acid agarose (QIAGEN), which was washed with a buffer of 10 mM Hepes (pH 7.5), 300 mM NaCl, 0.1% digitonin, and 10 mM imidazole (pH 7.5). Protein was eluted from the agarose with 300 mM imidazole. To remove the C-terminal GFP-His tag, thrombin was added to the eluate at a PANX1:thrombin

ratio of 1:100 (w/w) and incubated overnight. The protein was further purified by gel filtration with a Superose 6 Increase 10/300 GL column (GE Healthcare) in 10 mM Hepes (pH 7.5), 300 mM NaCl, and 0.05% digitonin buffer. The purified WT PANX1 proteins were analyzed by a protein sequencer [Procise 491 cLC (ABI) in Institute for Protein Research, Osaka University].

Nanodisc reconstitution of PANX1 channels in POPC lipid

Purified PANX1 channels were mixed with POPC (Avanti Polar Lipids) and MSP2N2 at a PANX1:MSP2N2:POPC molar ratio of 1:0.5:30 and placed on ice for 30 min. Bio-Beads SM-2 resin (Bio-Rad), which was washed in advance with the gel filtration buffer [10 mM Hepes (pH 7.5), 300 mM NaCl, and 0.05% digitonin], was added and incubated for 4 hours on a circular rotator. The supernatant was loaded onto a Superose 6 Increase 10/300 GL column in 10 mM Hepes (pH 7.5) and 300 mM NaCl buffer. The peak fractions were pooled and concentrated to 3 to 4 mg/ml for cryo-EM. For PANX-PBN, PBN sodium salt (P36400, Thermo Fisher Scientific) was solubilized in water and was directly added to the concentrated nanodisc solution of WT PANX1 to be finally 3 mM. The mixture was placed on ice for >1 hour and used for grid preparation.

Cryo-EM for PANX1 channels in nanodiscs

Molybdenum Quantifoil R2/2 200 mesh grids were preirradiated overnight with an electron beam and glow-discharged before use. The protein solution (1.5 μl) was placed on a grid, manually blotted for 10 s at room temperature, and plunged into liquid ethane with a manual plunger on a KF-80 (formerly Reichert-Jung).

For WT PANX1, PANX1-PBN, and PANX1ΔC379, the cryo-EM data were collected on a JEM-Z300FSC (CRYO ARM 300; JEOL Ltd., Akishima, Tokyo) that was operated at 300 kV at a nominal magnification of ×60,000. An in-column Omega energy filter was used for imaging (slit width, 30 eV). The microscope was equipped with a K3 camera (Gatan), and electron counting mode (5760 × 4092 pixels) with a pixel size of 0.81 Å was used. The exposure time was 2.6 s, resulting in a total dose of 50 $e^-/Å^2$ for WT PANX1 and 40 $e^-/Å^2$ for PANX1-PBN and PANX1ΔC379. Each image included 20 fractionated frames.

For PANX1ΔN20, the data were collected using a JEM-3000SFF (JEOL) at 300 kV equipped with a K2 summit (Gatan). The nominal magnification was ×40,600, and the specimen stage was maintained at about 100 K. The electron counting mode (3710 × 3838 pixels) with a pixel size of 1.232 Å was used. The exposure time was 8 s, resulting in the total dose of 56 $e^-/Å^2$, and each image included 40 fractionated frames.

The movie frames were aligned with MotionCor2 (*45*), and defocus was estimated using CTFFIND4 (*46*). Particles were boxed using EMAN2 (*47*) with a box size of 280 × 280 pixels for PANX1 WT, PANX1-PBN, and PANX1ΔC379 and 160 × 160 pixels for PANX1ΔN20. The processes described below were performed on RELION3.0 (*48*). After 2D classification, a stochastic gradient descent (SGD)–based initial model was generated. 3D classification was performed twice, and the final selected class provided a refined 3D reconstruction. Followed by contrast transfer function refinement and Bayesian polishing, the map was postprocessed with masking. The resolution was estimated by the gold standard Fourier shell correlation with a criterion of 0.143 (*49*). Local resolution maps were generated on ResMap (*50*).

Model building of PANX1 channels

The atomic model of PANX1 WT was manually built with Coot (*51*) and refined using PHENIX (*52*). For PANX1-PBN, the model of PANX1 WT was used as the initial model, and the N terminus of PANX1 WT was modified manually on Coot. The models of PANX1ΔC379 and PANX1ΔN20 were derived from those of PANX1 WT and PANX1-PBN, respectively. The secondary structure and noncrystallographic symmetry restraints were used through the PHENIX refinement. The structure statistics were evaluated using MolProbity (*53*), and the pore sizes of PANX1 channels were calculated using HOLE (*54*). PyMOL Molecular Graphics System (Schrödinger) and UCSF Chimera (*55*) were used to produce the figures.

MD simulations of WT PANX1 and PANX1-PBN

MD simulations were performed for WT PANX1 and PANX1-PBN in a similar manner. The structures of the missing atoms of the lipid molecules in the cryo-EM structures were modeled manually. The orientations of the PANX1 channels in the membrane were determined using the Positioning of Proteins in Membrane server (*56*). Each structure was then embedded in a solvated lipid bilayer using the CHARMM-GUI server (*57*, *58*) to generate a system composed of seven polypeptide chains, 363 to 371 POPC, about 150 mM KCl, and about 60,000 water molecules with dimensions of about 13 nm by 13 nm by 17 nm. The CHARMM36m force field parameters were used for the protein, lipid, and ions (*59*). The TIP3P model was used for water (*60*). After the system was energy-minimized and equilibrated, a 1-μs MD simulation was performed. During the MD simulations, the temperature was kept at 303.15 K using the Nosé-Hoover method (*61*, *62*), and the pressure was kept at 1.0×10^5 Pa using the Parrinello-Rahman method (*63*, *64*). Bond lengths involving hydrogen atoms were constrained using the linear constraint solver algorithm to allow the use of a large time step (2 fs) (*65*, *66*). Electrostatic interactions were calculated with the particle mesh Ewald method (*67*, *68*). MD simulations were performed with GROMACS 2020 (*69*), with coordinates recorded every 10 ps.

Electrophysiological analysis of PANX1 mutants with HEK whole-cell patch-clamp recordings and *Xenopus* oocyte voltage clamp recordings

Each fragment of the full-length or deletion mutants (PANX1ΔN20, PANX1ΔC379, and PANX1ΔN20ΔC379) was cloned into pIRES2-DsRed (Clontech) for patch-clamp recording and pGEM-HeFx for oocyte-clamp recording. HEK293T cells were cultured in Dulbecco's modified Eagle medium (Thermo Fisher Scientific) with 10% fetal bovine serum (MilliporeSigma) and 1% penicillin-streptomycin (Wako). Cells were seeded into glass bottom dishes at low concentrations 12 hours before transfection. Cells were transfected with plasmids using Lipofectamine 3000 (Thermo Fisher Scientific) according to the manufacturer's protocol. Patch-clamp recordings were performed on cells expressing the PANX1ΔC379 construct 18 to 24 hours after transfection because of the cytotoxicity of the construct and on cells expressing the other constructs 24 hours after transfection. Whole-cell voltage clamp recordings were performed using an EPC 10 USB patch-clamp amplifier and PATCHMASTER software (HEKA). DsRed fluorescent cells were selected for recording. Glass capillary microelectrodes with 3- to 5-megohm resistance were used. The pipette solution and bath solution contained the following: pipette solution, 145 mM NaCl, 10 mM EGTA, and 10 mM Hepes (pH 7.3) and bath solution, 160 mM NaCl, 3 mM KCl, 1 mM

$MgCl_2$, 2 mM $CaCl_2$, 13 mM glucose, and 10 mM Hepes (pH 7.4). The currents were low-pass–filtered at 1 kHz and sampled at 10 kHz. Voltage steps were applied (200 ms, 20-mV increments from −100 to +160 mV) from a holding potential of −60 mV.

The plasmids were linearized using restriction enzymes and then applied to an RNA preparation kit (T7 mMESSAGE mMACHINE, Thermo Fisher Scientific) according to the manufacturer's protocol. An adult *Xenopus laevis* female was anesthetized with MS-222 (Merck), and the ovarian lobes were collected using a surgical knife and forceps. The eggs were treated with type I collagenase solution (1 mg ml^{-1}; Thermo Fisher Scientific) in OR2 buffer (82.5 mM NaCl, 2 mM KCl, 1 mM $MgCl_2$, and 5 mM Hepes, adjusted to pH 7.5 using NaOH) at 18°C for 1.5 hours. Stage V and VI oocytes were collected manually and used for complementary RNA (cRNA) injection. cRNA (10 ng) for WT PANX1, PANX1ΔN20, and PANX1ΔN20ΔC379 or cRNA (1 ng) for PANX1ΔC379 was injected into *Xenopus* oocytes. For the negative control, only water was injected. Oocytes injected with cRNA were incubated for 2 days at 18°C in ND96 buffer (93.5 mM NaCl, 2 mM KCl, 1.8 mM $MgCl_2$, 2 mM $MgCl_2$, and 5 mM Hepes, adjusted to pH 7.5 using NaOH). Oocytes injected with cRNA for PANX1ΔC379 were incubated for 18 hours and used for the recording because the egg began to disintegrate 24 hours after injection. PANX channel currents were recorded using a Multi-Electrode Clamp Amplifier iTEV90. Glass capillary microelectrodes with 0.5- to 1.0-megohm resistance were used for current and voltage electrodes. The pipette solution contained 3 M KCl, 10 mM EGTA, and 10 mM Hepes (pH 7.4), and the bath solution contained ND96 buffer. To obtain the PANX1 channel current, the cells were initially clamped at −40 mV and then subjected to 2-s voltage steps from −20 to +60 mV in 20-mV increments. The four mutants of I41S, L45S, I118S, and L122S and the N-terminal deletions of these four mutants were generated with a site-directed mutagenesis protocol. The channel currents of the PANX1 mutants were investigated with *Xenopus* oocytes in the same way as described for WT PANX1. Data were analyzed by two-tailed Student's *t* test with $P < 0.05$ considered significant: $^{**}P < 0.01$ and $^{***}P < 0.001$.

Detection of PANX proteins on cell membranes of HEK293T and *Xenopus* oocytes

PANX1-transfected HEK293T cells were fixed with 4% paraformaldehyde (PFA) in phosphate-buffered saline (PBS), permeabilized with PBS with 0.1% Triton X-100 (PBST1), and blocked with 5% bovine serum albumin (BSA)/PBST1 at room temperature for 1 hour. Cells were subsequently hybridized with an antibody against human PANX1 (1:500; Proteintech) in blocking solution at 4°C overnight. Cells were then incubated with secondary anti-rabbit antibody conjugated to Alexa Fluor 488 (1:2000; Thermo Fisher Scientific) for 1 hour at room temperature. Fluorescence was examined under a BZ-X700 microscope (KEYENCE).

Oocytes were fixed with 4% PFA/PBS solution and embedded with OCT compound. Frozen sections were prepared on slide glass. The sections were permeabilized with PBST1 and blocked with 5% BSA/PBST1 at room temperature for 1 hour. Cells were subsequently hybridized with antibodies against human PANX1 (1:100; Proteintech) at 4°C overnight. Slices were incubated with secondary anti-rabbit antibody conjugated to Alexa Fluor 488 (1:1000; Thermo Fisher Scientific) for 3 hours at room temperature. Fluorescence was examined under a BZ-X700 microscope (KEYENCE). To distinguish fluorescent signals at the plasma membrane from yolk autofluorescence, we used a color camera along with a GFP long-pass filter.

SUPPLEMENTARY MATERIALS

www.science.org/doi/10.1126/scisignal.abg6941
Figs. S1 to S13
Tables S1 and S2
Movies S1 and S2
References (*70*–*72*)

View/request a protocol for this paper from *Bio-protocol*.

REFERENCES AND NOTES

1. S. Penuela, R. Gehi, D. W. Laird, The biochemistry and function of pannexin channels. *Biochim. Biophys. Acta* **1828**, 15–22 (2013).
2. S. Penuela, L. Harland, J. Simek, D. W. Laird, Pannexin channels and their links to human disease. *Biochem. J.* **461**, 371–381 (2014).
3. A. S. Lapato, S. K. Tiwari-Woodruff, Connexins and pannexins: At the junction of neuro-glial homeostasis & disease. *J. Neuro Res.* **96**, 31–44 (2018).
4. M. F. Santiago, J. Veliskova, N. K. Patel, S. E. Lutz, D. Caille, A. Charollais, P. Meda, E. Scemes, Targeting pannexin1 improves seizure outcome. *PLOS ONE* **6**, e25178 (2011).
5. J. X. Jiang, S. Penuela, Connexin and pannexin channels in cancer. *BMC Cell Biol.* **17**, 12 (2016).
6. P. W. Furlow, S. Zhang, T. D. Soong, N. Halberg, H. Goodarzi, C. Mangrum, Y. G. Wu, O. Elemento, S. F. Tavazoie, Mechanosensitive pannexin-1 channels mediate microvascular metastatic cell survival. *Nat. Cell Biol.* **17**, 943–952 (2015).
7. T. Freeman, S. Sayedyahossein, D. Johnston, R. Sanchez-Pupo, B. O'Donnell, K. Huang, Z. Lakhani, D. Nouri-Nejad, K. Barr, L. Harland, S. Latosinsky, A. Grant, L. Dagnino, S. Penuela, Inhibition of pannexin 1 reduces the tumorigenic properties of human melanoma cells. *Cancer* **11**, 102 (2019).
8. W. Silverman, S. Locovei, G. Dahl, Probenecid, a gout remedy, inhibits pannexin 1 channels. *Am. J. Physiol. Cell. Physiol.* **295**, C761–C767 (2008).
9. K. Michalski, T. Kawate, Carbenoxolone inhibits pannexin1 channels through interactions in the first extracellular loop. *J. Gen. Physiol.* **147**, 165–174 (2016).
10. L. Bao, S. Locovei, G. Dahl, Pannexin membrane channels are mechanosensitive conduits for ATP. *FEBS Lett.* **572**, 65–68 (2004).
11. R. J. Thompson, N. Zhou, B. A. MacVicar, Ischemia opens neuronal gap junction hemichannels. *Science* **312**, 924–927 (2006).
12. J. Wang, C. Ambrosi, F. Qiu, D. G. Jackson, G. Sosinsky, G. Dahl, The membrane protein pannexin1 forms two open-channel conformations depending on the mode of activation. *Sci. Signal.* **7**, ra69 (2014).
13. A. K. Narahari, A. J. Kreutzberger, P. S. Gaete, Y.-H. Chiu, S. A. Leonhardt, C. B. Medina, X. Jin, P. W. Oleniacz, V. Kiessling, P. Q. Barrett, K. S. Ravichandran, M. Yeager, J. E. Contreras, L. K. Tamm, D. A. Bayliss, ATP and large signaling metabolites flux through caspase-activated pannexin 1 channels. *eLife* **10**, e64787 (2021).
14. J. Wang, M. Ma, S. Locovei, R. W. Keane, G. Dahl, Modulation of membrane channel currents by gap junction protein mimetic peptides: Size matters. *Am. J. Physiol. Cell. Physiol.* **293**, C1112–C1119 (2007).
15. K. Michalski, J. L. Syrjanen, E. Henze, J. Kumpf, H. Furukawa, T. Kawate, The Cryo-EM structure of pannexin 1 reveals unique motifs for ion selection and inhibition. *eLife* **9**, e54670 (2020).
16. Z. Ruan, I. J. Orozco, J. Du, W. Lü, Structures of human pannexin 1 reveal ion pathways and mechanism of gating. *Nature* **584**, 646–651 (2020).
17. Z. Deng, Z. He, G. Maksaev, R. M. Bitter, M. Rau, J. A. J. Fitzpatrick, P. Yuan, Cryo-EM structures of the ATP release channel pannexin 1. *Nat. Struct. Mol. Biol.* **27**, 373–381 (2020).
18. R. Qu, L. Dong, J. Zhang, X. Yu, L. Wang, S. Zhu, Cryo-EM structure of human heptameric pannexin 1 channel. *Cell Res.* **30**, 446–448 (2020).
19. Q. Jin, B. Zhang, X. Zheng, N. Li, L. Xu, Y. Xie, F. Song, E. A. Bhat, Y. Chen, N. Gao, J. Guo, X. Zhang, S. Ye, Cryo-EM structures of human pannexin 1 channel. *Cell Res.* **30**, 449–451 (2020).
20. D. Deneka, M. Sawicka, A. K. M. Lam, C. Paulino, R. Dutzler, Structure of a volume-regulated anion channel of the LRRC8 family. *Nature* **558**, 254–259 (2018).
21. S. Maeda, S. Nakagawa, M. Suga, E. Yamashita, A. Oshima, Y. Fujiyoshi, T. Tsukihara, Structure of the connexin 26 gap junction channel at 3.5 Å resolution. *Nature* **458**, 597–602 (2009).
22. A. Oshima, K. Tani, Y. Fujiyoshi, Atomic structure of the innexin-6 gap junction channel determined by cryo-EM. *Nat. Commun.* **7**, 13681 (2016).
23. W. Choi, N. Clemente, W. Sun, J. Du, W. Lü, The structures and gating mechanism of human calcium homeostasis modulator 2. *Nature* **576**, 163–167 (2019).
24. K. Drożdżyk, M. Sawicka, M.-I. Bahamonde-Santos, Z. Jonas, D. Deneka, C. Albrecht, R. Dutzler, Cryo-EM structures and functional properties of CALHM channels of the human placenta. *eLife* **9**, e55853 (2020).

25. K. Demura, T. Kusakizako, W. Shihoya, M. Hiraizumi, K. Nomura, H. Shimada, K. Yamashita, T. Nishizawa, A. Taruno, O. Nureki, Cryo-EM structures of calcium homeostasis modulator channels in diverse oligomeric assemblies. *Sci. Adv.* **6**, eaba8105 (2020).
26. W. Yang, Y. Wang, J. Guo, L. He, Y. Zhou, H. Zheng, Z. Liu, P. Zhu, X. C. Zhang, Cryo-electron microscopy structure of CLHM1 ion channel from Caenorhabditis elegans. *Protein Sci.* **29**, 1803–1815 (2020).
27. A. N. Miller, S. B. Long, Crystal structure of the human two-pore domain potassium channel K2P1. *Science* **335**, 432–436 (2012).
28. S. G. Brohawn, E. B. Campbell, R. MacKinnon, Physical mechanism for gating and mechanosensitivity of the human TRAAK K^+ channel. *Nature* **516**, 126–130 (2014).
29. J. Payandeh, T. Scheuer, N. Zheng, W. A. Catterall, The crystal structure of a voltage-gated sodium channel. *Nature* **475**, 353–358 (2011).
30. B. Burendei, R. Shinozaki, M. Watanabe, T. Terada, K. Tani, Y. Fujiyoshi, A. Oshima, Cryo-EM structures of undocked innexin-6 hemichannels in phospholipids. *Sci. Adv.* **6**, eaax3157 (2020).
31. J. L. Syrjanen, K. Michalski, T.-H. Chou, T. Grant, S. Rao, N. Simorowski, S. J. Tucker, N. Grigorieff, H. Furukawa, Structure and assembly of calcium homeostasis modulator proteins. *Nat. Struct. Mol. Biol.* **27**, 150–159 (2020).
32. J. M. Kefauver, K. Saotome, A. E. Dubin, J. Pallesen, C. A. Cottrell, S. M. Cahalan, Z. Qiu, G. Hong, C. S. Crowley, T. Whitwam, W.-H. Lee, A. B. Ward, A. Patapoutian, Structure of the human volume regulated anion channel. *eLife* **7**, e38461 (2018).
33. G. Kasuya, T. Nakane, T. Yokoyama, Y. Jia, M. Inoue, K. Watanabe, R. Nakamura, T. Nishizawa, T. Kusakizako, A. Tsutsumi, H. Yanagisawa, N. Dohmae, M. Hattori, H. Ichijo, Z. Yan, M. Kikkawa, M. Shirouzu, R. Ishitani, O. Nureki, Cryo-EM structures of the human volume-regulated anion channel LRRC8. *Nat. Struct. Mol. Biol.* **25**, 797–804 (2018).
34. J. B. Myers, B. G. Haddad, S. E. O'Neill, D. S. Chorev, C. C. Yoshioka, C. V. Robinson, D. M. Zuckerman, S. L. Reichow, Structure of native lens connexin 46/50 intercellular channels by cryo-EM. *Nature* **564**, 372–377 (2018).
35. X. Xu, L. E. Wicki-Stordeur, J. C. Sanchez-Arias, M. Liu, M. S. Weaver, C. S. W. Choi, L. A. Swayne, Probenecid disrupts a novel pannexin 1-collapsin response mediator protein 2 interaction and increases microtubule stability. *Front. Cell. Neurosci.* **12**, 124 (2018).
36. J. W. Kyle, P. J. Minogue, B. C. Thomas, D. A. L. Domowicz, V. M. Berthoud, D. A. Hanck, E. C. Beyer, An intact connexin N-terminus is required for function but not gap junction formation. *J. Cell Sci.* **121**, 2744–2750 (2008).
37. F. B. Chekeni, M. R. Elliott, J. K. Sandilos, S. F. Walk, J. M. Kinchen, E. R. Lazarowski, A. J. Armstrong, S. Penuela, D. W. Laird, G. S. Salvesen, B. E. Isakson, D. A. Bayliss, K. S. Ravichandran, Pannexin 1 channels mediate "find-me" signal release and membrane permeability during apoptosis. *Nature* **467**, 863–867 (2010).
38. A. Oshima, K. Tani, M. M. Toloue, Y. Hiroaki, A. Smock, S. Inukai, A. Cone, B. J. Nicholson, G. E. Sosinsky, Y. Fujiyoshi, Asymmetric configurations and N-terminal rearrangements in Connexin26 gap junction channels. *J. Mol. Biol.* **405**, 724–735 (2011).
39. H.-J. Lee, H. Jeong, J. Hyun, B. Ryu, K. Park, H.-H. Lim, J. Yoo, J.-S. Woo, Cryo-EM structure of human Cx31.3/GJC3 connexin hemichannel. *Sci. Adv.* **6**, eaba4996 (2020).
40. R. Bruzzone, S. G. Hormuzdi, M. T. Barbe, A. Herb, H. Monyer, Pannexins, a family of gap junction proteins expressed in brain. *Proc. Natl. Acad. Sci. U.S.A.* **100**, 13644–13649 (2003).
41. D. G. Jackson, J. Wang, R. W. Keane, E. Scemes, G. Dahl, ATP and potassium ions: A deadly combination for astrocytes. *Sci. Rep.* **4**, 4576 (2014).
42. A. Oshima, T. Matsuzawa, K. Nishikawa, Y. Fujiyoshi, Oligomeric structure and functional characterization of Caenorhabditis elegans innexin-6 gap junction protein. *J. Biol. Chem.* **288**, 10513–10521 (2013).
43. Q. Shao, Q. Liu, R. Lorentz, X.-Q. Gong, D. Bai, G. S. Shaw, D. W. Laird, Structure and functional studies of N-terminal Cx43 mutants linked to oculodentodigital dysplasia. *MBoC.* **23**, 3312–3321 (2012).
44. A. Dukkipati, H. H. Park, D. Waghray, S. Fischer, K. C. Garcia, BacMam system for high-level expression of recombinant soluble and membrane glycoproteins for structural studies. *Protein Expr. Purif.* **62**, 160–170 (2008).
45. S. Q. Zheng, E. Palovcak, J.-P. Armache, K. A. Verba, Y. Cheng, D. A. Agard, MotionCor2: Anisotropic correction of beam-induced motion for improved cryo-electron microscopy. *Nat. Methods* **14**, 331–332 (2017).
46. A. Rohou, N. Grigorieff, CTFFIND4: Fast and accurate defocus estimation from electron micrographs. *J. Struct. Biol.* **192**, 216–221 (2015).
47. G. Tang, L. Peng, P. R. Baldwin, D. S. Mann, W. Jiang, I. Rees, S. J. Ludtke, EMAN2: An extensible image processing suite for electron microscopy. *J. Struct. Biol.* **157**, 38–46 (2007).
48. J. Zivanov, T. Nakane, B. O. Forsberg, D. Kimanius, W. J. Hagen, E. Lindahl, S. H. Scheres, New tools for automated high-resolution cryo-EM structure determination in RELION-3. *eLife* **7**, e42166 (2018).
49. P. B. Rosental, R. Henderson, Optimal determination of particle orientation, absolute hand, and contrast loss in single-particle electron cryomicroscopy. *J. Mol. Biol.* **333**, 721–745 (2003).
50. A. Kucukelbir, F. J. Sigworth, H. D. Tagare, Quantifying the local resolution of cryo-EM density maps. *Nat. Methods* **11**, 63–65 (2014).
51. P. Emsley, B. Lohkamp, W. G. Scott, K. Cowtan, Features and development of Coot. *Acta Crystallogr. D Biol. Crystallogr.* **66**, 486–501 (2010).
52. P. D. Adams, P. V. Afonine, G. Bunkóczi, V. B. Chen, I. W. Davis, N. Echols, J. J. Headd, L.-W. Hung, G. J. Kapral, R. W. Grosse-Kunstleve, A. J. McCoy, N. W. Moriarty, R. Oeffner, R. J. Read, D. C. Richardson, J. S. Richardson, T. C. Terwilliger, P. H. Zwart, PHENIX: A comprehensive Python-based system for macromolecular structure solution. *Acta Crystallogr. D. Biol. Cryst.* **66**, 213–221 (2010).
53. V. B. Chen, W. B. Arendall III, J. J. Headd, D. A. Keedy, R. M. Immormino, G. J. Kapral, L. W. Murray, J. S. Richardson, D. C. Richardson, MolProbity: All-atom structure validation for macromolecular crystallography. *Acta Crystallogr. D. Biol. Cryst.* **66**, 12–21 (2010).
54. O. S. Smart, J. G. Neduvelil, X. Wang, B. A. Wallace, M. S. Sansom, HOLE: A program for the analysis of the pore dimensions of ion channel structural models. *J. Mol. Graph.* **14**, 354–360 (1996).
55. E. F. Pettersen, T. D. Goddard, C. C. Huang, G. S. Couch, D. M. Greenblatt, E. C. Meng, T. E. Ferrin, UCSF Chimera: A visualization system for exploratory research and analysis. *J. Comput. Chem.* **25**, 1605–1612 (2004).
56. M. A. Lomize, I. D. Pogozheva, H. Joo, H. I. Mosberg, A. L. Lomize, OPM database and PPM web server: Resources for positioning of proteins in membranes. *Nucleic Acids Res.* **40**, D370–D376 (2012).
57. S. Jo, T. Kim, V. G. Iyer, W. Im, CHARMM-GUI: A web-based graphical user interface for CHARMM. *J. Comput. Chem.* **29**, 1859–1865 (2008).
58. E. L. Wu, X. Cheng, S. Jo, H. Rui, K. C. Song, E. M. Dávila-Contreras, Y. Qi, J. Lee, V. Monje-Galvan, R. M. Venable, J. B. Klauda, W. Im, CHARMM-GUI membrane builder toward realistic biological membrane simulations. *J. Comput. Chem.* **35**, 1997–2004 (2014).
59. J. Huang, S. Rauscher, G. Nawrocki, T. Ran, M. Feig, B. L. de Groot, H. Grubmüller, A. D. MacKerell Jr., CHARMM36m: An improved force field for folded and intrinsically disordered proteins. *Nat. Methods* **14**, 71–73 (2017).
60. W. L. Jorgensen, J. Chandrasekhar, J. D. Madura, R. W. Impey, M. L. Klein, Comparison of simple potential functions for simulating liquid water. *J. Chem. Phys.* **79**, 926–935 (1983).
61. W. G. Hoover, Canonical dynamics: Equilibrium phase-space distributions. *Phys. Rev. A* **31**, 1695–1697 (1985).
62. S. Nose, A molecular dynamics method for simulations in the canonical ensemble. *Mol. Phys.* **52**, 255–268 (1984).
63. S. Nose, M. L. Klein, Constant pressure molecular dynamics for molecular systems. *Mol. Phys.* **50**, 1055–1076 (1983).
64. M. Parrinello, A. Rahman, Polymorphic transitions in single crystals: A new molecular dynamics method. *J. Appl. Phys.* **52**, 7182–7190 (1981).
65. B. Hess, H. Bekker, H. J. C. Berendsen, J. G. E. M. Fraaije, LINCS: A linear constraint solver for molecular simulations. *J. Comput. Chem.* **18**, 1463–1472 (1997).
66. B. Hess, P-LINCS: A parallel linear constraint solver for molecular simulation. *J. Chem. Theory Comput.* **4**, 116–122 (2008).
67. T. Darden, D. York, L. Pedersen, Particle mesh Ewald: An *N*·log(*N*) method for Ewald sums in large systems. *J. Chem. Phys.* **98**, 10089–10092 (1993).
68. U. Essmann, L. Perera, M. L. Berkowitz, T. Darden, H. Lee, L. G. Pedersen, A smooth particle mesh Ewald method. *J. Chem. Phys.* **103**, 8577–8593 (1995).
69. B. Hess, C. Kutzner, D. van der Spoel, E. Lindahl, GROMACS 4: Algorithms for highly efficient, load-balanced, and scalable molecular simulation. *J. Chem. Theory Comput.* **4**, 435–447 (2008).
70. J. D. Thompson, D. G. Higgins, T. J. Gibson, CLUSTAL W: Improving the sensitivity of progressive multiple sequence alignment through sequence weighting, position-specific gap penalties and weight matrix choice. *Nucleic Acids Res.* **22**, 4673–4680 (1994).
71. L. Mou, M. Ke, M. Song, Y. Shan, Q. Xiao, Q. Liu, J. Li, K. Sun, L. Pu, L. Guo, J. Geng, J. Wu, D. Deng, Structural basis for gating mechanism of pannexin 1 channel. *Cell Res.* **30**, 452–454 (2020).
72. S. Zhang, B. Yuan, J. H. Lam, J. Zhou, X. Zhou, G. Ramos-Mandujano, X. Tian, Y. Liu, R. Han, Y. Li, X. Gao, M. Li, M. Yang, Structure of the full-length human Pannexin1 channel and insights into its role in pyroptosis. *Cell Discovery* **7**, 30 (2021).

Acknowledgments: We are grateful to H. Iwao (JEOL) for maintaining the electron microscopes at Nagoya University. We thank K. Tanaka (Nagoya University) for creating movies of MD simulations. **Funding:** This work was supported by Grants-in-Aid for Scientific Research (B) under grant number JP17H03683 (M.W.) and Challenging Research (Exploratory) (K.T.); the Platform Project for Supporting Drug Discovery and Life Science Research [Basis for Supporting Innovative Drug Discovery and Life Science Research (BINDS)] from Agency for Medical Research and Development (AMED) under grant numbers JP21am0101118 (K.T.), JP21am0101107 (support number 3135) (T.T.), JP20ae0101050, and JP21am0101074; Grants-in-Aid for Scientific Research (B) under grant number 19H03165; Grants-in-Aid for Challenging Exploratory Research under grant number 21K19215, the Naito Foundation and

Daiko Foundation (A.O.); Foreign Young Invited Research Unit (B-2) from Nagoya University (A.O. and T.F.); and Grants-in-Aid for Scientific Research (S), the Japan New Energy and Industrial Technology Development Organization (NEDO), and the Japan AMED (Y.F.). This work was partially supported by the Nagoya University Research Fund. **Author contributions:** M.K. and H.H. expressed and purified the proteins and generated the nanodisc reconstitution. K.H., K.K., and A.O. collected cryo-EM data. A.O. and K.T. processed cryo-EM images and performed model building and refinement. M.W. measured channel activity with electrophysiology. T.T., M.I.M., and F.T. contributed to MD simulations. A.O. designed and supervised the research. A.O., K.T., M.W., and Y.F. contributed to writing the paper. **Competing interests:** The authors declare that they have no competing interests. **Data and materials availability:** Cryo-EM density maps for nanodisc reconstituted PANX1 channels were deposited in the EM Data Bank (www.emdatabank.org) under accession codes EMD-31489 (WT PANX1), EMD-31491 (PANX1ΔC379), EMD-31492 (PANX1ΔN20), and EMD-31490 (PANX1-PBN). Atomic coordinates were deposited in the PDB under accession numbers 7F8J, 7F8O, 7F8Q, and 7F8N. Cryo-EM images were deposited in the Electron Microscopy Pilot Image Archive (EMPIAR; www.ebi.ac.uk/pdbe/emdb/empiar) with accession codes EMPIAR-10757, EMPIAR-10758, EMPIAR-10759, and EMPIAR-10760.

Submitted 22 January 2021
Accepted 21 December 2021
Published 8 February 2022
10.1126/scisignal.abg6941

Science Signaling

Structures of human pannexin-1 in nanodiscs reveal gating mediated by dynamic movement of the N terminus and phospholipids

Maki Kuzuya, Hidemi Hirano, Kenichi Hayashida, Masakatsu Watanabe, Kazumi Kobayashi, Tohru Terada, Md. Iqbal Mahmood, Florence Tama, Kazutoshi Tani, Yoshinori Fujiyoshi, and Atsunori Oshima

Sci. Signal., **15** (720), eabg6941.
DOI: 10.1126/scisignal.abg6941

A protein domain and lipids at the gate

The large-pore, multisubunit channel pannexin-1 (PANX1) enables permeation of ions, metabolites, and second messengers, such as ATP, across the plasma membrane. Kuzuya *et al*. generated structures of wild-type, mutant, and pharmacologically inhibited channels by cryo–electron microscopy (see the Focus by Anderson and Thompson). Combined with electrophysiological analysis and molecular dynamics simulations, these studies showed that gating of this large-pore channel was determined by movement of the intracellular N terminus and, subsequently, the diffusion of lipids into or out of the pore. Understanding the gating of PANX-1 may lead to ways to manipulate channel activity, which plays a role in pain sensation and cancer metastasis.

Science Signaling (ISSN) is published by the American Association for the Advancement of Science. 1200 New York Avenue NW, Washington, DC 20005. The title *Science Signaling* is a registered trademark of AAAS.